Acoustic Microscopy Characterization of Highly-Ordered Anodized Nanoporous Alumina Films for Nanotechnology Applications

Pooja Dubey, Nico Declercq, Min Zhai, Alexandre Locquet, Mi Jung, Deokha Woo, D.S. Citrin

Acoustic Microscopy Characterization of Highly-Ordered Anodized Nanoporous Alumina Films for Nanotechnology Applications

Pooja Dubey[a,b,*], Nico F. Declercq[a,b], Min Zhai[b,c], Alexandre Locquet[b,c], Mi Jung [d], Deokha Woo[e], D. S. Citrin[b,c]

[a] *George W. Woodruff School of Mechanical Engineering, Georgia Institute of Technology, North Avenue, Atlanta, 30332, Georgia, United States*
[b] *Georgia Tech-CNRS IRL2958, Georgia Tech-Europe, 2 Rue Marconi, 57070 Metz, France*
[c] *School of Electrical and Computer Engineering, Georgia Institute of Technology, North Avenue, Atlanta, 30332-0250, Georgia, United States*
[d] *Konkuk University Global Campus, 268 Chungcheonbuk-do, 27478, Republic of Korea*
[e] *Sensor System Research Center, Korea Institute of Science and Technology, Seoul, Republic of Korea*

Abstract

The acoustic properties of a well-aligned nanoporous alumina (NP Al_2O_3) film synthesized through a two-step anodization process have been characterized nondestructively using scanning acoustic microscopy (SAM). In particular, leaky surface-acoustic-wave (SAW) modes were investigated on the film, and a comparison was carried out between the material properties of uniform and non-uniform nanoporous Al_2O_3 films. The Rayleigh velocity for $V(z)$ of the various scanning areas was estimated while simulations were performed to validate the experimental results. The non-uniform surface morphology of nanoporous Al_2O_3 is also validated by polarized-resolved terahertz time-domain spectroscopy (THz TDS).

Keywords: Scanning Acoustic Microscopy (SAM), Aluminium oxide, nanostructured film

I. Introduction

The novel class of nanoporous (NP) materials are promising in applications ranging from sensing [1, 2], catalysis [3], biomedical engineering [3, 4], and energy harvesting [5, 6] to nanocomposite coatings [7-10] owing to the ability to tune physical properties beyond those of the constituent bulk materials, such as low macroscopic density, high surface-to-volume (S/V) ratio, and controllability of the porosity. Specifically, NP Al_2O_3 films have attracted attention due to their chemical and physical properties (such as optical responsiveness, photoluminescence, dielectric properties), simple manufacturing process, and low cost [11].

Due to interest in applications of NP Al_2O_3, there has been a focus on the evolution of film surface morphology and NP pattern formation [12-15]. A typical NP Al_2O_3 film is of thickness 60-70 μm. Despite numerous investigations on characterizing NP materials, most only focus on optical techniques. Of interest to the current work are earlier studies [16, 17] in which the homogeneity and anisotropy of NP Al_2O_3 films on Al substrates were characterized nondestructively by terahertz (THz) imaging and THz spectroscopy. The observed rough surface morphology and anisotropy based on the THz results were validated by cross-sectional field emission scanning electron microscopy (FE-SEM), atomic force microscopy (AFM), and x-ray diffraction (XRD).

In contrast to optical methods, ultrasonic acoustic waves target the mechanics of the materials. Indeed, ultrasonics is one of the well-known methods of investigating the mechanical properties of materials nondestructively [18-21]. There have been limited ultrasonic studies of NP Al_2O_3 films. Ultrasonic

*Corresponding author.
Email address: pooja.dubey@gatech.edu (Pooja Dubey)

characterization of alumina layers of up to 3.5 μm thickness in reflection demonstrate the applicability of this technique for the investigation of thin Al_2O_3 layers [22, 23]. Ultrasonic transmission using a conventional MHz transducer has been applied to characterize the elastic properties of NP Al_2O_3 films [24]. Still, these techniques may not be capable of measuring sub-micron thicknesses due to the high-frequency requirements. On the other hand, scanning acoustic microscopy (SAM), exploiting the requisite higher frequencies, has been widely used to date to study the acoustic properties in biological and opaque materials [25-29]. In 1985, Kushibiki et al. [30] demonstrated, using SAM, the ability to study layered and thin-film samples, and highlighted the material characterization techniques using Rayleigh velocity curves $V(z)$ measurements with z the distance from the transducer to the sample. Such measurements record the output voltage of the acoustic transducer varying with z. The periodicity of the dips present in $V(z)$ is closely related to the Rayleigh velocity on the surface of the sample [31, 32]. SAM was also applied to determine phosphoric acid-anodized oxide Al_2O_3 films of 1 to 22 μm thickness [22]. It successfully demonstrated SAM as a promising tool for determining mechanical properties, such as the density and elasticity of the layer. The technique was also used to estimate the near-surface elastic properties to model depth-varying properties [33].

However, none of the existing literature reported the acoustic properties of NP films or explored the use of ultrasonics to characterize such materials. Thus, in this paper, NP Al_2O_3 thin films fabricated by a two-step electrochemical anodization are characterized nondestructively using SAM. The ultrasonic analysis is conducted to assess the elastic properties of NP Al_2O_3 films. A comparative study with destructive FE-SEM and THz measurements is also conducted. These analyses open the door to developing NP materials with a focus on acoustic or other mechanical properties.

II. Specimen

The investigated NP Al_2O_3 films are fabricated through a two-step anodization process; the detailed process flow is shown in Fig. 1. Compared to conventional one-step and pre-pattern anodization, the self-organized NP Al_2O_3 films are more uniform and regular on Al substrates [34, 35]. Before the anodization process, electro-polishing is employed in a mixed solution of $HClO_4$: C_2H_5OH with 1:4 in volume for 60 s to remove initial surface oxides and reduce the surface roughness of the Al foil. Subsequently, the first anodization is carried out in 0.3 M $H_2C_2O_4$ at 3°C. The first anodization's duration and bias voltage are set to ~8 h and 40 V, respectively. An 80 μm NP Al_2O_3 film with a ~20 μm nonuniform layer on the top and a uniform layer on the bottom is formed on the Al substrate.

In order to improve the regularity of the NP arrangement, the disordered NP Al_2O_3 film is removed using wet chemical etching with a 0.2 M CrO_3 and 0.4 M $4H_3PO_4$ solution at ~65 °C for ~6 h. A patterned hexagonal array of concave structures remains on the Al substrate after the dissolution of NP Al_2O_3 layers formed during the first anodization. These patterns serve as the template for NP formation in the second anodization.

The second anodization is carried out using the same apparatus and under the same conditions as the first anodization, such as temperature (~3°C), the concentration of reaction solution (0.3 M $H_2C_2O_4$), and bias voltage (40 V). Well-ordered NP Al_2O_3 films on the Al substrate is observed. Structural parameter values, such as interpore distance and pore diameter, are obtained based on the field-emission scanning electron microscopy (FE-SEM, Hitachi S-4700) results, which are 105±5 nm and 33±3 nm, respectively.

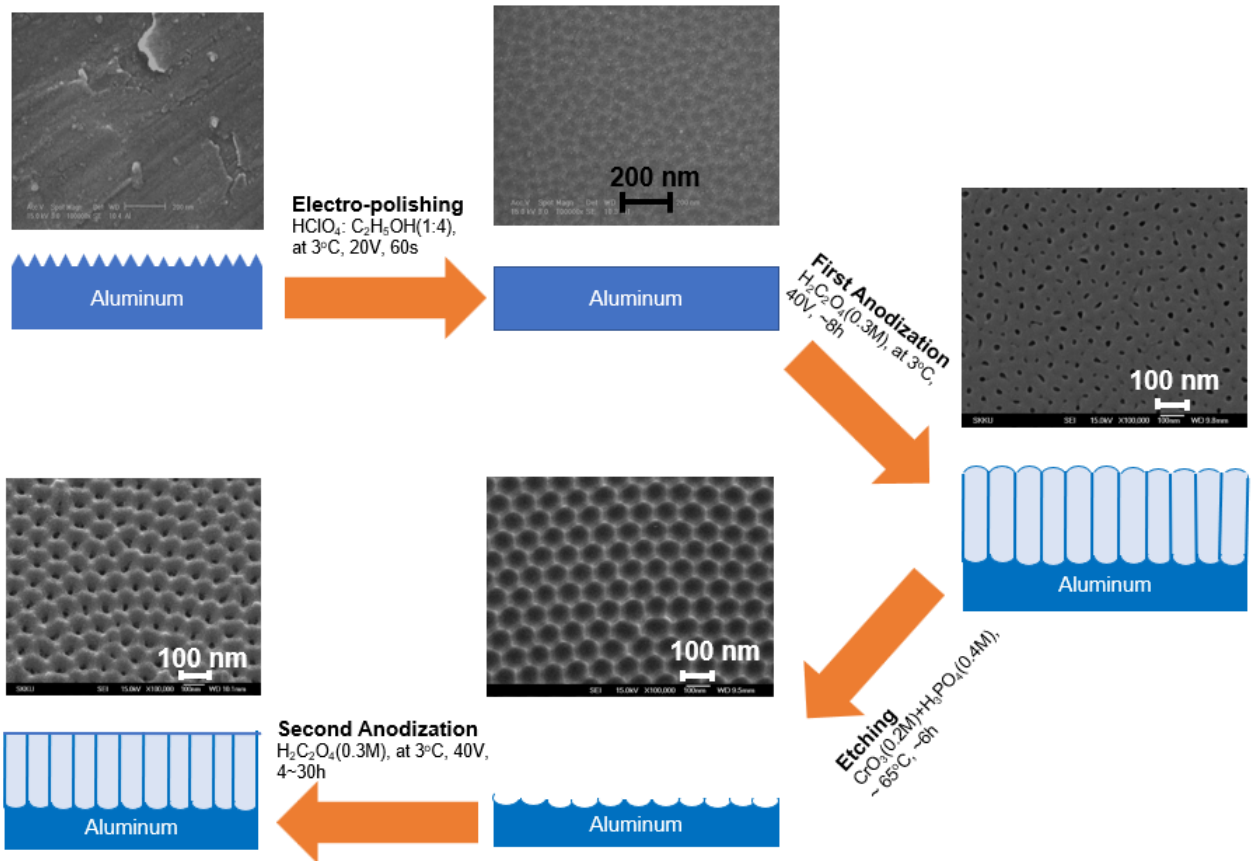

Fig. 1. The process flow of the second step anodization for the self-ordered anodized NP Al_2O_3 films. Representative top-view FE-SEM micrographs under different phases are also shown.

III. Experimental Procedure

A. Scanning Acoustic Microscopy

A SAM setup (ELSAM, Ernst-Leitz Scanning Acoustic Microscope; PVA TePla Analytical Systems, GMBH, Deutschordenstrasse 38, 73463 Westhausen, Germany) is employed in this work. The measurements are carried out with a 400 MHz lens having an axial resolution of 1.88 µm and an aperture diameter of 0.3 mm. The focal length of the lens for water is 0.3 mm. For the V(z) analysis mentioned in the next section GHz-SAM Control Software for ELSAM is used and for processing of the data, MATLAB is used.

The experimental procedure involves the use of acoustic micrographs representing the image formed due to the reflection (because of the acoustic impedance mismatch) of ultrasound waves at sample interfaces. For the study, acoustic micrographs are obtained at *z* focus (z_0) for the NP Al_2O_3 with various thicknesses present on the Al substrate (Fig. 2(a)). Other measurements are made with only Al substrate. Thus, the technique facilitates differentiation between areas with and areas without film. The probed area under consideration for the study is of the dimension 500 µm x 500 µm. The interference of the non-specular sound field caused by leaky, *i.e.*, re-radiating, Rayleigh waves at the surface with the specular reflected bulk waves from the sample provides contrast to the images.

Furthermore, an investigation of the variation of surface and interface waves with the change in the defocusing distance *z* of the lens is carried out to retrieve information about the material properties. The data is recorded as *V*(*z*); these curves give the received voltage at the acoustic microscopy lens (consisting of the

piezoelectric element and the acoustic lens system) as a function of distance *z* between the acoustic probe and the sample (Fig. 2).

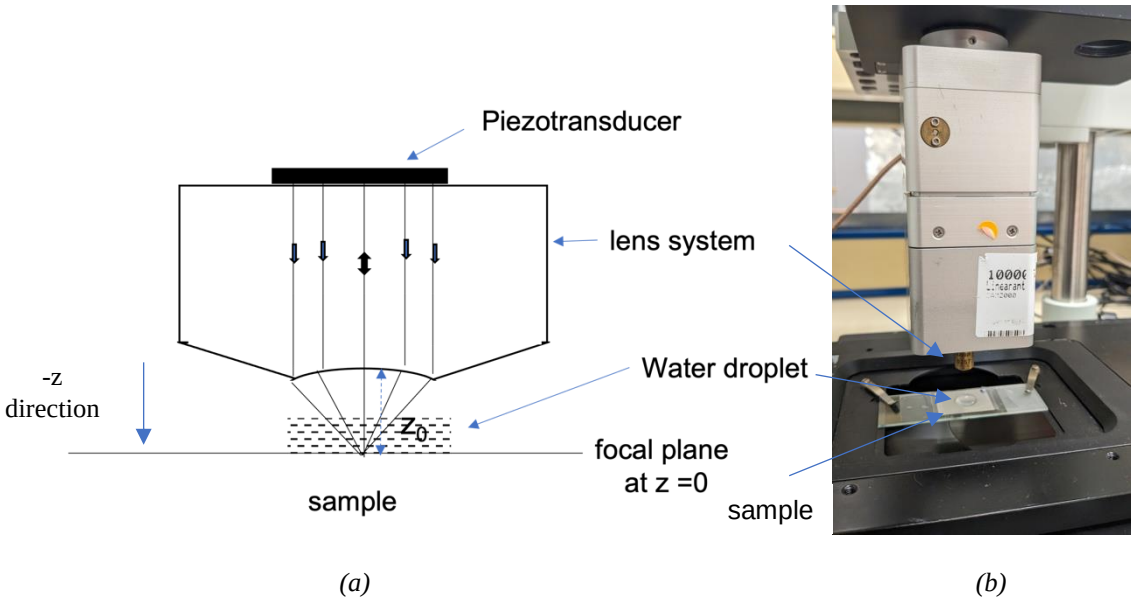

Fig. 2. (a) Schematic of the lens system with the sample in reflection acoustic microscope (b) Sample with lens system mounted in the acoustic microscope setup.

The *V*(*z*) output is a superimposition of reflected waves from the sample and the leaky waves on the sample surface. A typical *V*(*z*) curve contains oscillations/ripples as the transducer is moved in the -*z* direction. These are formed due to the phase difference between the superimposed signals [36]. In case of thin layers and coatings, the curves provide insight into the micro-elastic properties of the coating and its interaction with the substrate. The interference of the non-specular sound field caused by leaky, *i.e.*, re-radiating, Rayleigh waves at the surface with the specular reflected bulk waves from the sample provides contrast to the images.

The surface acoustic wave (SAW) velocity (c_{SAW}) is calculated using Eq. (1) [30] where c_w , f, and Δz represent the speed of sound in water, the frequency of the input, and the oscillation period in the *V(z)* curve as a function of distance z in between lens and sample,

$$c_{SAW} = \frac{c_w}{\sqrt{1-\left(1-\frac{c_w}{2f\Delta z}\right)^2}}. \quad (1)$$

IV. Results

A. Experimental Results

1. Analysis using acoustic micrographs

The acoustic micrographs, or SAM images, obtained for various NP Al_2O_3-film thicknesses, shown in Fig. 3(b)-(e), are compared with the acoustic micrograph of the Al substrate, in Fig. 3(a). A clear distinction in contrast and pattern is visible in the acoustic micrographs indicating the variation in the mechanical properties of the NP Al_2O_3 film as compared to the Al substrate [37].

As the maximum resolution obtained for the measurements using 400 MHz is ~ 2.5 µm, the nanopores in

the film are not visible in the scans. Thus, macroscopic characterization is obtained from the $V(z)$ scans.

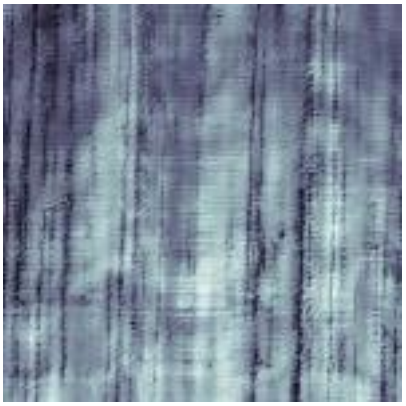

(a)

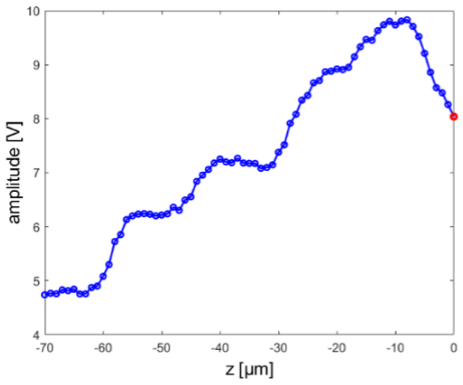

(f)

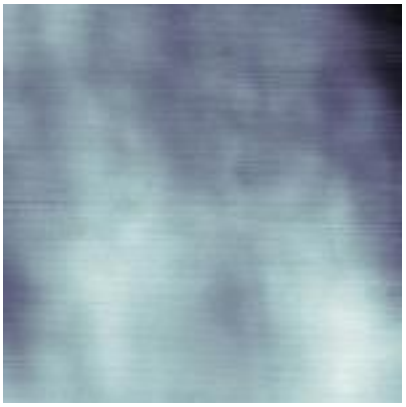

(b)

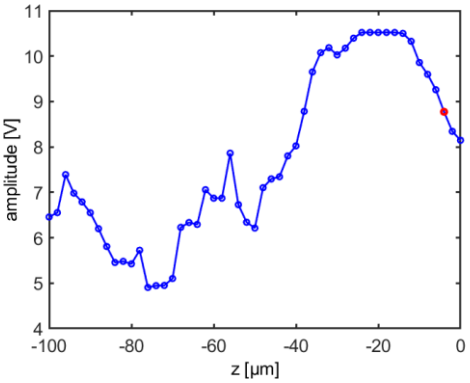

(g)

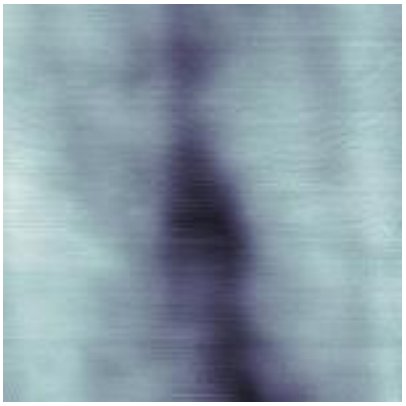

(c)

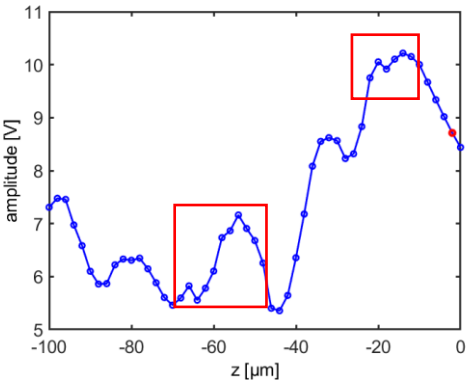

(h)

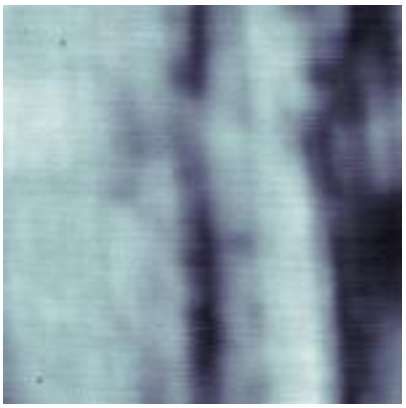

(d)

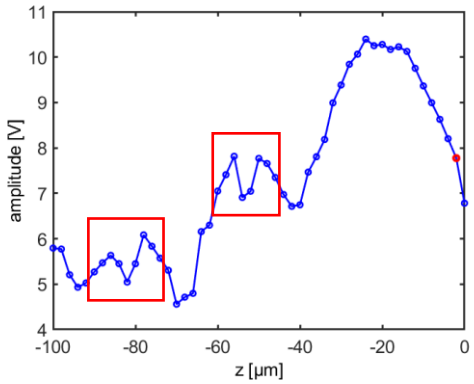

(i)

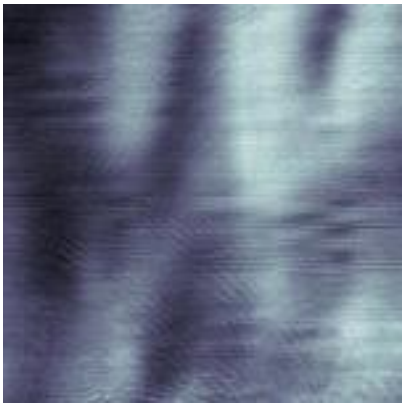

(e)

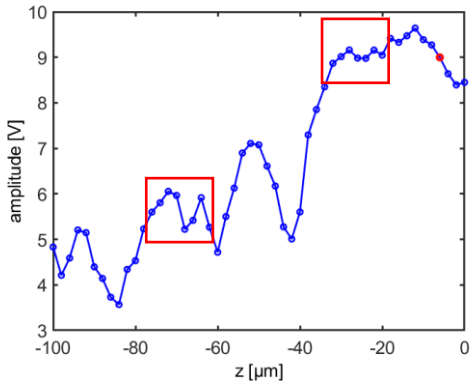

(j)

Fig. 3. Acoustic micrograph of (a) the Al substrate and the NP Al_2O_3 film on an Al substrate with a thickness of (b) 12 μm, (c) 30 μm, (d) 50 μm, and (e) 60 μm. (f)-(j) *V*(*z*) of the micrograph in the Fig. 3(a)-(e) respectively. The SAM acquisition is carried out with an acoustic lens of frequency 400 MHz.

2. Analysis using *V*(*z*) curves

V(*z*) is measured for the NP Al_2O_3 films of various thicknesses. In the paper, *V*(*z*) curves shown are averaged over all pixels (*x*,*y*) on the micrograph. The maximum defocus distance, which defines the depth from *z* focus (z_0) point in the -*z* direction is limited to 100 μm at 400 MHz (See Fig. 2(a)). Distilled water is used as a coupling medium in the experiment. The water temperature is maintained in the range 20-24° C. It has been observed that *V*(*z*) from the samples contain the ripples (as described in section III.A) due to the detection of SAWs on the surface, and therefore, a frequency of 400 MHz works well to investigate the sample.

V(*z*) is analyzed using signal-processing software to determine the unique acoustic signature associated with the leaky waves propagating on the liquid/NP Al_2O_3 film interface. Two types of leaky modes are visible (highlighted in red) in *V*(*z*) for the samples of thickness 30, 50, and 60 μm (Fig. 3(h)-(j)) as compared with *V*(*z*) for the bare Al substrate (Fig. 3(b)). This observation of two leaky modes correlates directly with the investigation on phosphoric acid-anodized Al_2O_3 film by Zinin *et al*. [22] using acoustic microscopy. Also, as pointed out by earlier studies [26, 38], the high-velocity mode is due to the longitudinal waves propagating

parallel to the sample surface. This mode is explained with respect to the level of roughness of the film and would not be visible for a perfectly smooth sample. Eventually as roughness increases, the longitudinal velocity becomes comparable to the SAW velocity and is observed in $V(z)$ [22].

The processing of $V(z)$ is carried out according to the ray model for a spherical lens proposed in Briggs [39]. This is a Fourier-transform-based approach to determine the acoustic properties from $V(z)$. Pre-processing of the $V(z)$ signals involves isolating Rayleigh ripples from the curves. This step includes filtering of the raw $V(z)$ from reverberation effects due to the lens. It is implemented in the I-III step shown in the flowchart (Fig. 4(a)). First, the fast ripples or water ripples are removed by using a moving average filter with window length of $\frac{\lambda_w}{2}$ where λ_w corresponds to wavelength of ultrasound waves in water. The second part includes removing the interference due to the lens. It is achieved in step I using $V(z)$ obtained from reference material Pb (perfect acoustic reflector).

Based on the ray-theory approximation, the exponentially decaying part in the intermediate function can be approximated as the Rayleigh component. Then, the Rayleigh parameters are extracted using the Fourier transform and then performing a least-squares fit to minimize any other unwanted effects (residual offset, head wave contribution) (Step III and IV in Fig. 4(a)). The obtained set of wavenumbers is then linked to estimate the periodicity or dip interval of $V(z)$ curve (Δz) (Eq. (2)) and thus obtain c_{SAW}. A flowchart showing the brief experimental procedure is provided in Fig. 4; however, for deeper understanding of each step, the reader is referred to Briggs [39]. Additionally, all the stages of processing with description are shown in Addendum A. Physically, the technique is based on the added phase in the reradiated sound field instigated by the extra propagation distance caused by the conversion of incident bulk waves into SAWs and then back to reradiated or leaky sound. This added phase results in the phase difference between re-radiated sound and specular reflected sound and causes the interference ripples seen in $V(z)$. Extraction of the implied phase difference provides the SAW velocity.

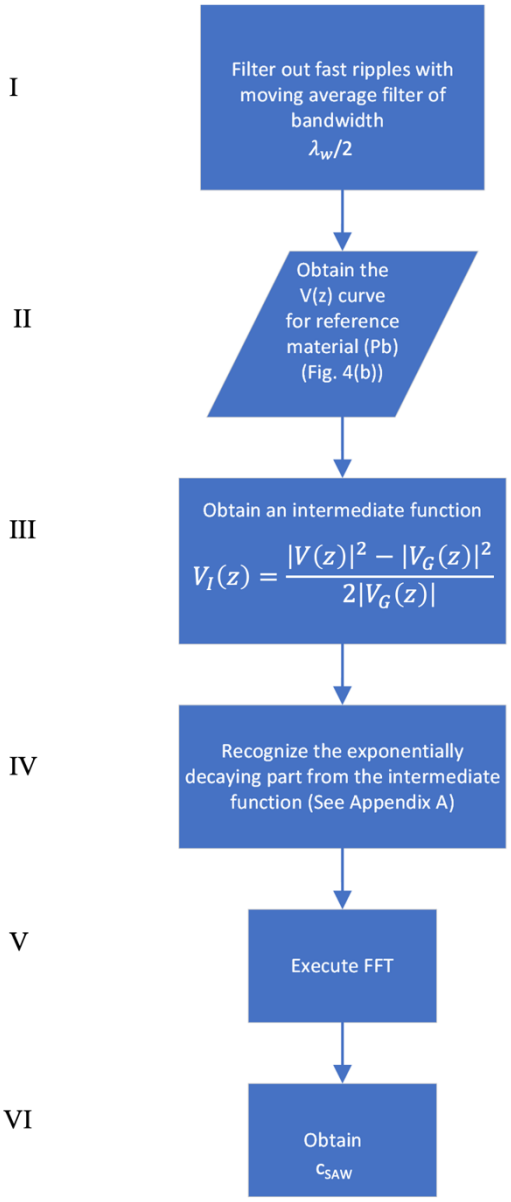

Fig. 4. (a) Flowchart of the experimental procedure for processing $V(z)$.

Figs. 5(b) and 5(c) show the post-processing results for a NP Al_2O_3 film with thickness of 50 µm. The region of interest in the micrograph is highlighted in red (Fig. 5(a)). As per the above mentioned procedure, the dip interval (Δz) is calculated using the values obtained from the spectral analysis of the $V(z)$ curve for various NP Al_2O_3 film thicknesses [30] using Eq. (2),

$$\Delta z(n) = \frac{2\pi}{\zeta(n)}. \tag{2}$$

In Eq. (3), ζ is the maximum amplitude at the center frequency in the $V(z)$ curve for the n^{th} leaky mode. The peaks in the plot (Fig. 4(c)) shows the different leaky wave modes present for the mentioned sample under consideration.

The Rayleigh-wave velocity of the bare Al substrate is obtained and compared with known results to

calibrate the SAM measurements. The measured $V_I(z)$ curve obtained for a bare Al sample using Eq. (2), and its spectrum is shown in Figs. 5(a) and 5(b). The SAW velocity (c_{SAW}) using Eqs. (1) and (2) give $c_{SAW} =$ 2981.45 m/s, corresponding to the value found in the literature which is 2960 m/s [40].

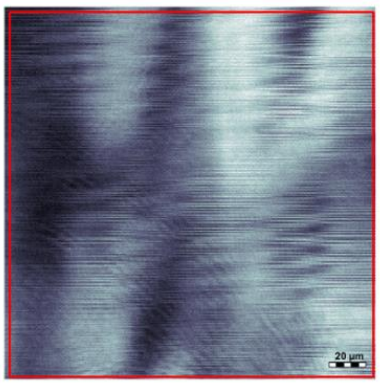

(a)

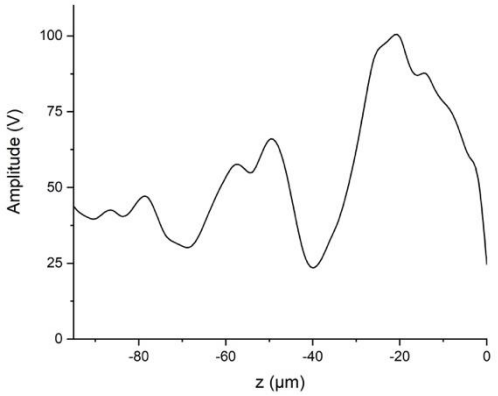

(b)

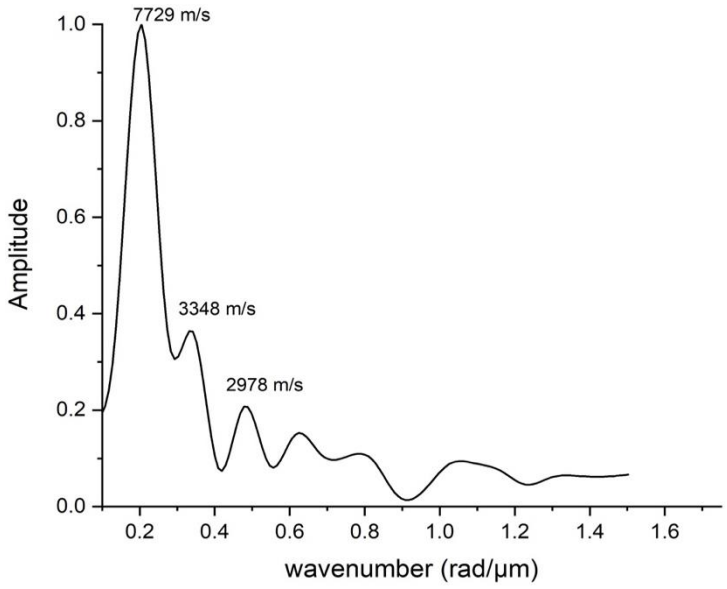

(c)

Fig. 5. (a) Micrograph with region of interest (shown in red) obtained for a NP Al_2O_3 layer with thickness 50 µm on an Al substrate. (b) Intermediate function obtained by processing of *V*(*z*) of Fig. 5(a) (step V) in Fig 4(a). (c) Spectrum of the curve obtained in Fig. 5(b) (step VI in Fig. 4(a)) corresponding to the highlighted region of interest. The speed of sound c_{SAW} for each peak corresponding to the wavenumber is also shown above the respective peak.

The next part of the investigation is carried out on the sample of film thickness 50 µm. *V*(*z*) for the 500 µm x 500 µm scan area is obtained. Two leaky modes (peaks in Fig. 5(c)) are observed. One of them is a high-velocity mode of 7729 m/s, and another a comparatively low-velocity mode of 3348 m/s.The highest value is consistently present in all the other samples (with thickness 12, 30, and 60 µm) as well, indicating the velocity is not affected by the film thickness. Therefore, it is attributed to a bulk acoustic mode and its value matches that of longitudinal bulk waves. Thus, based on the obtained value, for the numerical simulation, the layer's longitudinal velocity is 7729 m/s. The value is similar to the longitudinal velocity of

8200 m/s as determined for 90 µm thick, porous oxalic-acid-anodized (OAA) Al oxide film [41]. The experimental results for bulk Al_2O_3 [42], OAA oxide film, and phosphoric-acid-anodized (PAA) porous Al oxide film from the literature are given in Table 1. Based on the similarity in the range of the values in Table I, the second leaky mode obtained in the experimental results is inferred to be the Rayleigh wave velocity c_R of the film by excluding other possibilities. Had we assumed the low-velocity leaky mode to be the shear velocity of the film, according to Eq. (4), the calculated value of Rayleigh wave velocity would have resulted in 3354 m/s which is not present in the spectrum shown in Fig. 5(c). This assumption-negation technique confirms the argument that the low-velocity mode is the Rayleigh wave velocity. The experimental results for NP Al_2O_3 film are observed to be different from porous PAA oxide films [41]. Presumably, this is due to the regular and well-ordered distribution of nanopores in the NP Al_2O_3 film under investigation, as compared to the fairly uniform distribution in the porous films. Additionally, the size of the pores in the sample under investigation is much smaller than the wavelength of the ultrasonic waves used for the experiment minimizing diffraction effects.

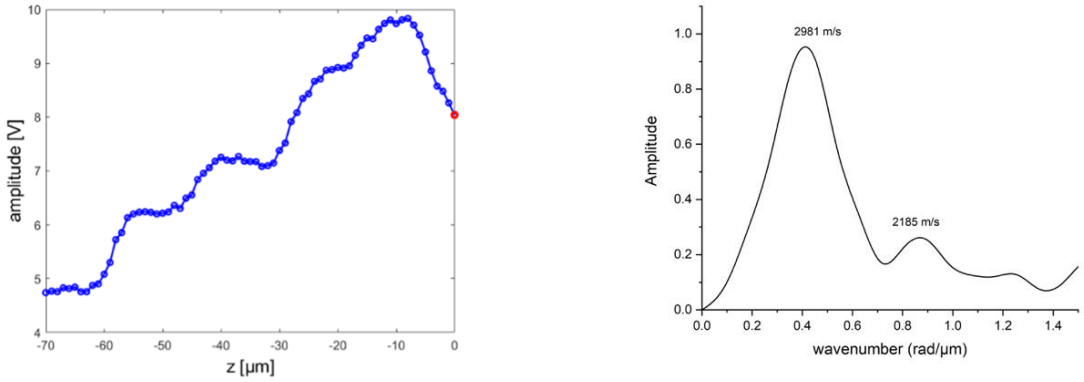

(a) *(b)*

Fig. 6. (a) *V*(*z*) for the Al substrate (shown in Fig. 3(a) and (b)). (b) The spectrum of *V*(*z*) in (a).

Table 1: Experimental values for longitudinal, shear, and Rayleigh wave velocity and its comparison with other literature.

Film	c_l (m/s)	c_R (m/s)	c_t (m/s)
NP Al_2O_3[a]	7729	3546	3348
OAA film	8200[b]	-	3610
PAA film[c]	5500	3540	3200
Bulk Al_2O_3[d]	10700	6360	5690

[a] Based on acoustic microscopic measurements for 50 µm thick film.

[b] Based on normal incidence reflection coefficient measurements [41].

[c] Based on acoustic microscopic measurement on 12 µm thick film [22].

[d] Based on reflection calculations on a liquid-solid interface using Schoch displacement for an Al oxide with ρ of 4000 $\mathrm{kg/m^3}$[42] .

The Rayleigh velocity obtained for the NP Al_2O_3 film is c_R = 3546 $\mathrm{m/s}$. To further estimate the material properties of the layer, the shear-wave velocity (c_t) is computed. For the calculation, it is assumed that the layer is isotropic, and the SAW energy is concentrated in the layer due to sufficient film thickness. Thus, by using the equation of Farnell [43], the value of c_t is obtained from

$$\frac{c_R}{c_t} = \frac{0.72 - \left(\frac{c_t}{c_l}\right)^2}{0.75 - \left(\frac{c_t}{c_l}\right)^2}. \tag{3}$$

Based on the Rayleigh-wave velocity c_R found above, the shear velocity c_t is 3348 $\mathrm{m/s}$. Thus, for further investigation of the mechanical properties of this thin layer, we assume that the sample obeys classical linear elastic theory. The model helps relate the bulk isotropic material properties, such as the elastic modulus (*E*) and the Poisson ratio (ν), to the material's longitudinal velocity c_l and shear-wave velocity c_t by

$$E = \frac{3 - 4\left(\frac{c_t}{c_l}\right)}{1 - \left(\frac{c_t}{c_l}\right)^2} \rho c_t^2, \tag{4}$$

$$\nu = \frac{2\left(\frac{c_t}{c_l}\right)^2 - 1}{2\left[\left(\frac{c_t}{c_l}\right)^2 - 1\right]}. \tag{5}$$

where ρ is the density. Since the density of NP OAA oxide film is always less than the solid OAA oxide film, the value of ρ must be less than 2850 $\mathrm{kg/m^3}$. Based on the existing literature on porous OAA Al_2O_3, the density is assumed to be in range of 2200−2700 $\mathrm{kg/m^3}$ [41]. Thus, the value of ν using the experimental c_l and c_t is 0.37. The value of *E* based on Eq. (4) for a range of assumed density is shown in Fig. 7.

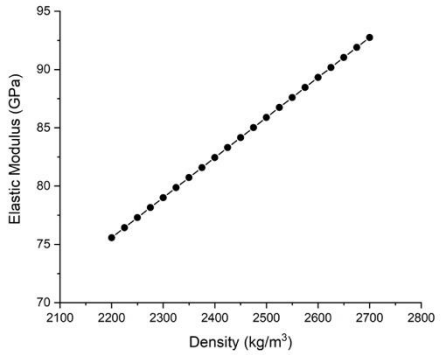

Fig. 7. Elastic modulus E, obtained for different density values.

Fifteen measurements are recorded at 400 MHz for a 50 µm NP Al_2O_3 film with scan area 500 µm x 500 µm. The computed standard deviation in the Rayleigh-wave velocity for these fifteen measurements is found out to be 48 $\mathrm{m/s}$ (with a confidence interval of 95 %). Next, a set of 80 randomly selected regions of interest of various areas (described below) for the 50 µm thick film is considered for the statistical analysis. The area

of these regions varied from 17.5 µm x 17.5 µm to 500 µm x 500 µm. A few of those regions are shown in Fig. 8. For each region, an average $V(z)$ curve is obtained. Fig. 9 shows the distribution of the Rayleigh velocity for all the region of interest varying in area. The computed mean for all the samples is 3353 m/s, with a standard deviation of 82 m/s.

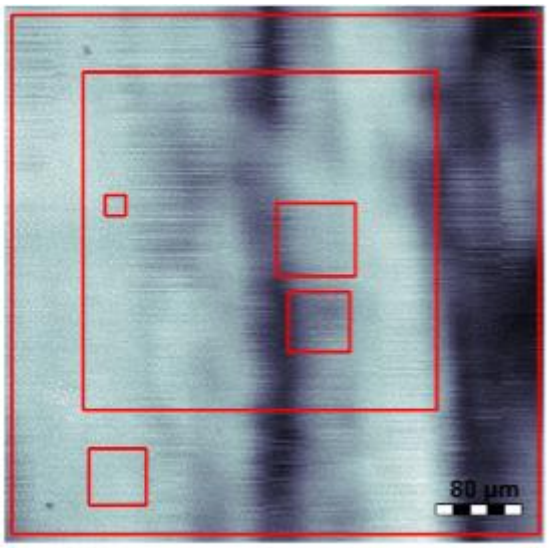

Fig. 8. A few of the regions (highlighted in red) from among 80 randomly chosen regions of interest for analysis. The regions comprise of different areas size. The complete micrograph of NP Al_2O_3 film shown is of the dimension 500 µm x 500 µm.

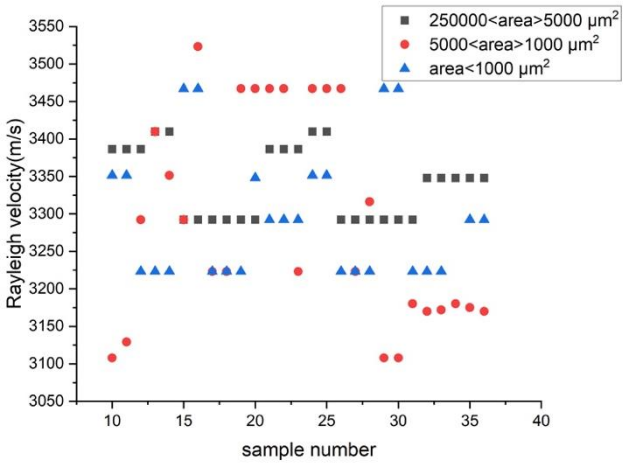

Fig. 9. Scatter plot of Rayleigh velocity for samples for regions of different areas.

Fig. 10(a) shows the histogram for 80 samples with their Rayleigh velocity, fitted with the normal distribution curve. The mean of the distribution is 3296 m/s, which deviates from the obtained mean for the same size region of interest by 52 m/s. Furthermore, Fig. 10(b) shows a probability plot of the Rayleigh velocity, which follows an almost straight line indicating very few departures from the fitted distribution curve. Based on the figure, it can also be concluded that the distribution fit contains the maximum points within the 95% confidence band with only a few outliers. The standard deviation after fitting the data is 84 m/s, compared with the results with only a single scan area of 500 µm x 500 µm (carried out in the earlier part), which was 49 m/s. The variation could result from non-uniformity on the film's surface. The observation indicates that this technique may be used for nondestructive uniformity evaluation, because the average value of c_R was dependent on the size and location of the investigated region which can only be caused by non-uniformity. This non-uniformity in acoustic impedance is at a scale at least as large as the focus wavelength (1.85µm) and focal spot size 1.88 µm.

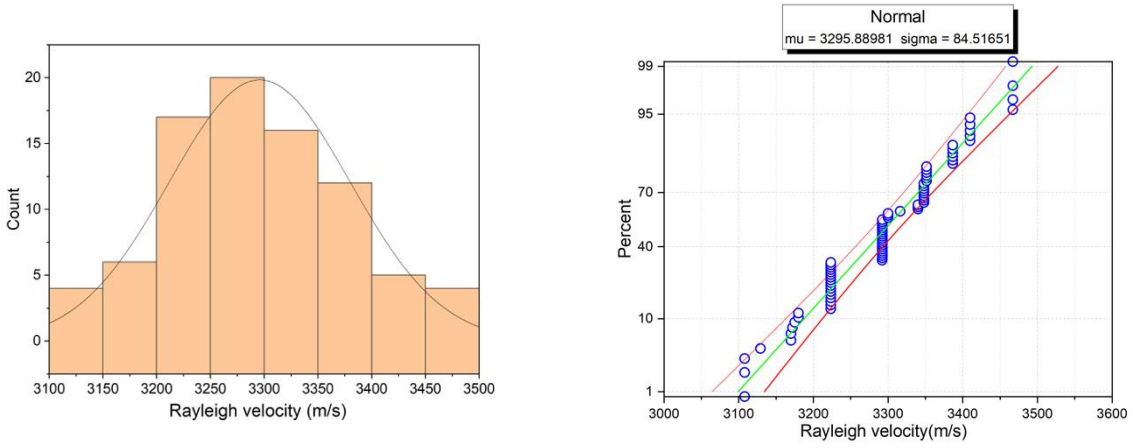

(a) *(b)*

Fig. 10. (a) $V(z)$ for the bare Al substrate is shown in FIG. 3(a). (b) The spectrum of $V(z)$ in (a). The histogram shows the Rayleigh velocity for samples with various regions of interest. (b) Probability plot depicting the Rayleigh velocity and the 95 % confidence level (shown by red lines).

B. Simulations

The numerical analysis for the leaky wave is performed using Disperse™ [44]. The film is modeled as a homogeneous, isotropic layer of Al_2O_3 with the experimental values of c_l and c_t. The numerical simulations were carried out for the ρ values range of $2200-2700\ \mathrm{kg/m^3}$. The Rayleigh-wave velocity predicted using the numerical simulation for an isotropic film thickness of 50 µm assuming the density to be $2500\ \mathrm{kg/m^3}$ was found to be $3319\ \mathrm{m/s}$ which agrees with the experimental velocity of $3348\ \mathrm{m/s}$. The observed difference in the values must be due to the isotropic characteristic of the modelled film.

V. Terahertz experiments

THz reflectometry was subsequently carried out to provide additional information on the NP Al_2O_3 films. For example, using the technique of THz time-of-flight tomography, an independent and nondestructive measurement of the film thickness can be obtained. The THz measurements are based on a commercial pulsed THz time-domain spectroscopy (TDS) system (TPS Spectra 3000 from TeraView LTD, Cambridge, UK). The generation of THz pulses is based on optically pumping a photoconductive switch. Quasi-single-cycle THz pulses with an effective band from 60 GHz to 3 THz are generated in a biased GaAs antenna after excitation by an Er-doped fiber laser emitting sub-100-fs 780-nm pulses at a 100 MHz repetition rate with average output power >65 mW. Coherent detection of the THz radiation is performed in a similar photoconductive antenna circuit by gating the photoconductive gap with sub-100-fs 780-nm pulses synchronized to the THz emission. A delay line is incorporated into the probe beam to change the difference in the optical delay between the incoming THz pulse and the probe laser pulse at the receiver. A bias is also applied across the emitter and receiver to generate a time-gated output signal. By taking the Fourier transform of the detected THz signal subsequent to interaction with the sample, the THz spectrum can be obtained. The recorded temporal reflected THz signal contains 4096 data points (corresponding sample period T_s is 0.0116 ps) and is averaged over 10 shots per pixel to reduce the effect of noise. The depth of focus (roughly the Rayleigh length z_R) is ~ 7 mm and thus the beam waist is approximately constant over the depth of the sample. the transverse resolution (beam waist for a Gaussian beam) $w_0 = (\lambda z_R/n\pi)^{1/2}$ is ~580 µm at 1 THz (taking n=1 in air).

Fig. 11 (a) shows the reflected signal from NP Al_2O_3 film with a nominal thickness of 60 µm. Ripples on

the baseline originate from water-vapor absorption [2] and can be corrected for in the data analysis. Moreover, two positive echoes arising from the air/NP Al_2O_3, and NP Al_2O_3 /Al interfaces, are visually distinguished in time. The thickness of NP Al_2O_3 film at that pixel can be calculated based on the optical delay between these two positive echoes, which is ~56.6 μm, showing agreement with the value obtained from cross-sectional FE-SEM in Fig. 11(b). Of note, cross-sectional FE-SEM, as a destructive method, only gives the thickness information along with the cross-section profile and fails to provide the thickness distribution of the entire surface.

Except for thickness measurements, uniformity associated with non-specular scattering, as well as anisotropy of NP Al_2O_3 film, are also studied nondestructively using THz scattering imaging and polarization-resolved THz TDS. In general, the birefringence of porous materials is related to the crystal structure, lattice arrangement, and structural parameters, such as porosity [21] and pore size [45]. We refer the reader to [16, 17] for the detailed discussion on birefringence as well as the regularity of the surface morphology of the NP Al_2O_3 films.

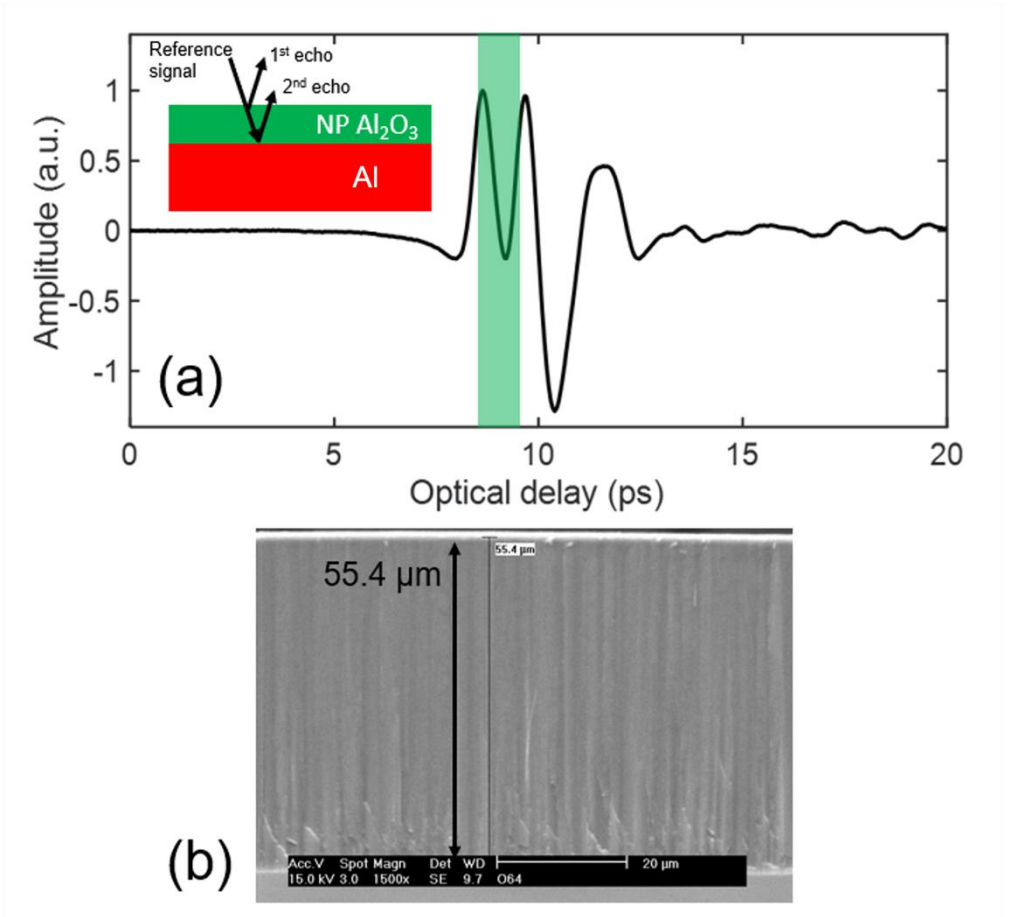

Fig. 11. (a) Typical temporal reflected signal from NP Al_2O_3 film with a nominal thickness of 60 μm. Inset shows the origin of the two positive echoes in the reflected THz signal: one from the air/ NP Al_2O_3 interface and the second from the NP Al_2O_3/Al interface. (b) The cross-section FE-SEM result of investigated NP Al_2O_3 film.

VI. Conclusion

The study successfully characterizes the highly ordered NP Al_2O_3 isotropic films formed on Al substrates using SAM. The material properties such as Elastic modulus and Poison ratio were computed based on the technique utilizing the Rayleigh-wave mode and the longitudinal mode in the V(z) curves. The elastic modulus thus obtained ranges from 75 to 92 GPa with a density variation from 2200 kg/m^3 to 2700 kg/m^3. The Poison ratio for the film is 0.37. The Rayleigh-wave velocity estimated for the NP Al_2O_3 film is 3348 m/s. Investigation into the Rayleigh-wave velocity changes for the NP Al_2O_3 is shown. The nonuniform surface morphology after the two-step anodization process of the film is observed and it was shown that it is sufficiently sensitive to serve as a nondestructive uniformity evaluation tool for such samples. THz reflectivity experiments provide nondestructive verification of the film thicknesses. Previous THz measurements[16, 17] also indicate significant nonuniformity in portions of the films.

Acknowledgement

Conseil Régional Grand Est, France, and CPER SusChemProc, France, supported this work.

Addendum

A. Stages of processing of *V*(*z*)

It is based on the method proposed by Briggs [46] for spherical lens analysis. One of the prominent features of *V*(*z*) is the presence of oscillations with negative defocus. The periodicity of the oscillations is related to Rayleigh-wave velocity using Snell's law given in Eq. (1). Based on the ray model, the received signal at the transducer has two components, one of which contributes to the Rayleigh surface-wave velocity $V_R(z)$ and another because of the surface geometry and characteristics of the lens $V_G(z)$. The output $V(z)$ is related as shown by the expression in Eq. A(1). In the equation, $\emptyset(\boldsymbol{z})$ represents the phase angle between V_G and V_R:

$$|\mathbf{V}|^2 = |\mathbf{V_G}|^2 + |\mathbf{V_R}|^2 + 2|\boldsymbol{V_G}||\boldsymbol{V_R}|\boldsymbol{cos}\emptyset. \qquad \boldsymbol{A(1)}$$

Usually, a perfect reflector such as Pb or Au is considered as a reference material to characterize the lens property ($V_L(z) \sim V_G(z)$). After extracting the $|V_R|$ component, further processing, such as FFT, is performed, and the acoustical parameters relating to material properties are computed. For instance, the stages of processing are described for 50 µm NP $\mathbf{Al_2O_3}$ film shown in Fig. A.1(a) with its *V*(*z*) measurement in Fig. A.1(b).

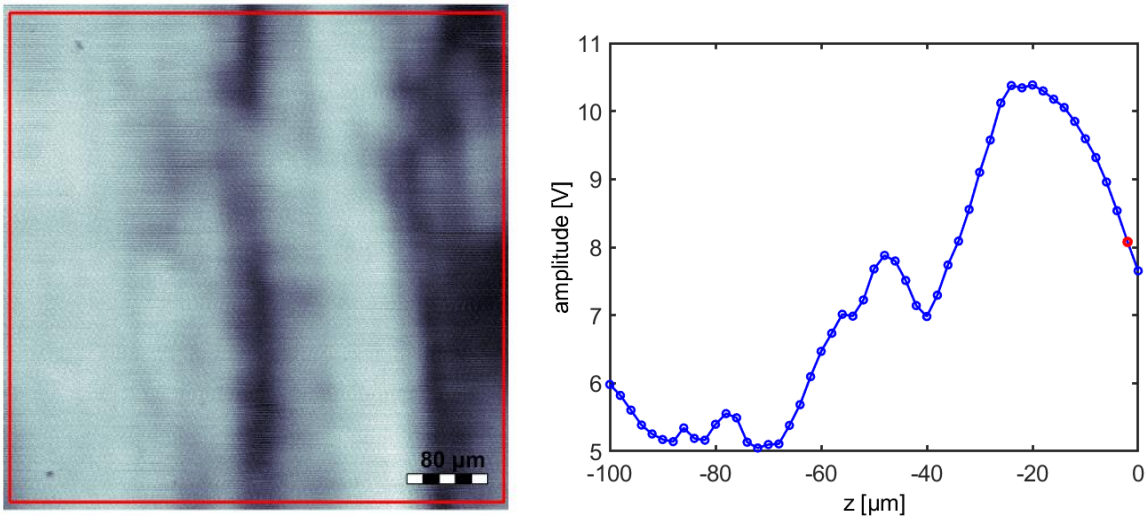

Fig. A.1 (a) Micrograph with the region of interest (shown in red) obtained for a NP $\mathbf{Al_2O_3}$ layer with a thickness of 50 µm on a bare **Al** substrate. (b) $V(z)$ obtained a NP $\mathbf{Al_2O_3}$ layer with a thickness of 50 µm on a bare Al substrate.

1. Filtering out of the water ripples using a moving average filter with a bandwidth $\frac{\lambda_w}{2}$ where $\boldsymbol{\lambda_w}$ corresponds to the wavelength of ultrasound waves in water. This process smoothens the measured $V(z)$ and removes fast ripples. The step is shown in Fig. A.2.

2. The second part includes filtering $V(z)$ data to eliminate interference due to lens characteristics.

   a) To obtain this, the $V_L(z)$ is experimentally recorded for lead (Fig. A.3).

   b) An intermediate function is calculated in order to simplify the estimation of the expression in Eq. A(2). The graphical result is shown in Fig. A.4,

$$\boldsymbol{V_I(z) = \frac{|V(z)|^2 - |V_G(z)|^2}{2|V_G(z)|}}. \qquad \boldsymbol{A(2)}$$

   c) The term $|V_R(z)|\cos\emptyset(z)$ in Eq. (6) makes it difficult to calculate the expression for a spherical lens exactly. However, according to the ray model, $V_R(z)$ is an exponentially decaying component. Thus, the exponential decaying part is recognized from the intermediate calculation (shown by a dashed line in Fig. A.4(a)).

3. The Fourier transform of the chosen exponential part and obtained results show the spatial frequency or wavenumber present. The wavenumbers are further linked with the dip interval given by Eq. (2). Results are shown in Fig. A.5(b). (When FFT is performed on the entire intermediate function (2(b)), the transform shows many other lower velocity modes (Fig. A.5(a)) due to lens interference effects.

4. The velocity of leaky waves (c_{SAW}) is then computed from Eq. (1) using the results in the previous step.

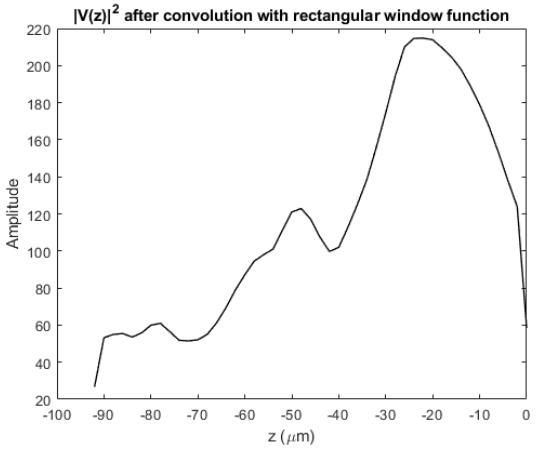

Fig. A.2 Signal obtained after filtering the square of $|V(z)|$ by a moving average filter with bandwidth $\frac{\lambda_w}{2}$.

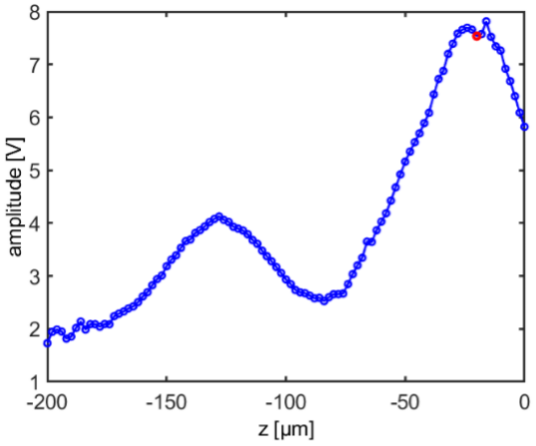

Fig. A.3 $V(z)$ of reference material (Pb) obtained with a 400 MHz frequency.

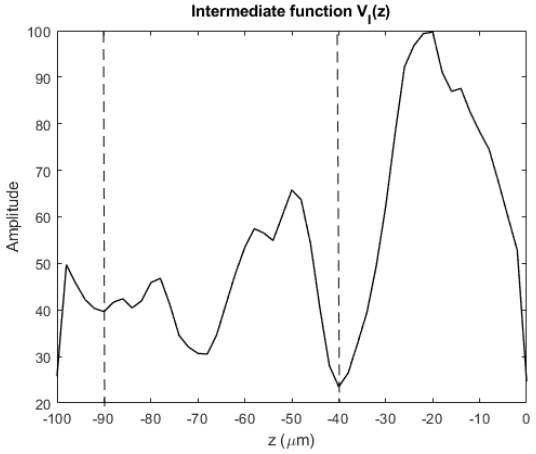

Fig. A.4 Intermediate function obtained by processing of the $V(z)$ curve in Fig. A.2 using Eq. (7). The dashed line in the figure shows the exponentially decaying part chosen for processing the FFT. The exponential decaying part represents the $|V_R|$ as per the ray model.

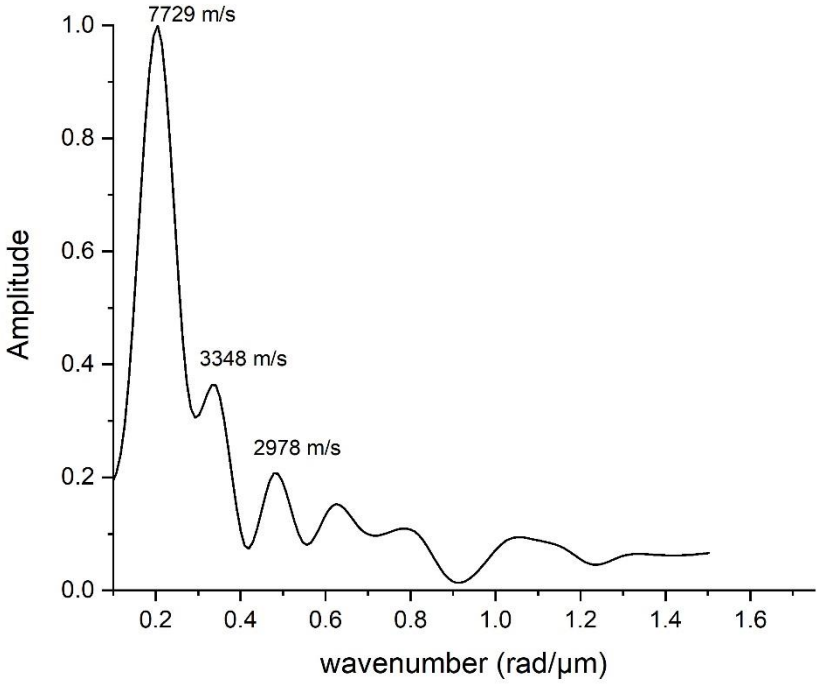

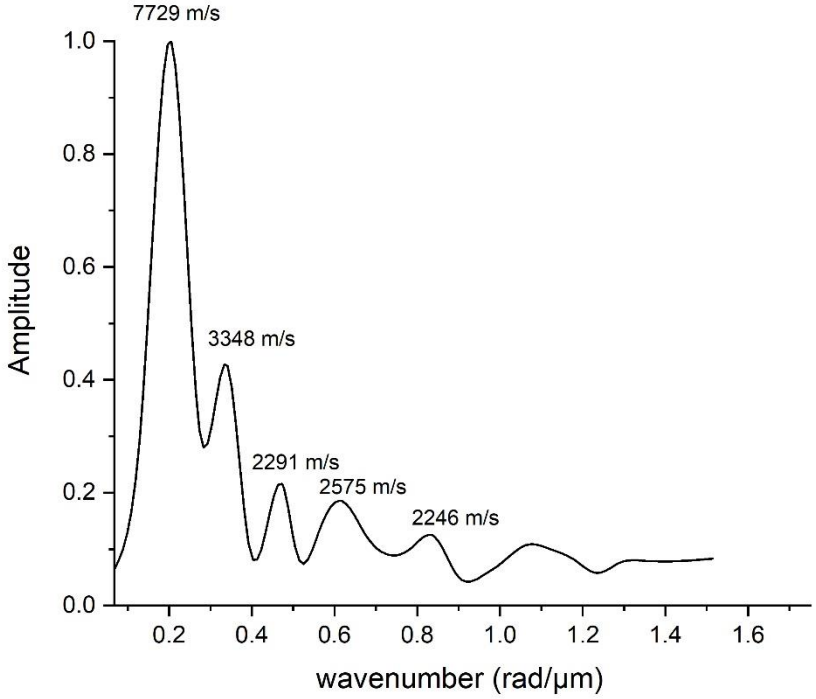

Fig. A.5 (a) The spectrum of the exponentially decaying part represented by dashed lines in Fig. A.4. (b) The spectrum of the complete intermediate function shown in Fig. A.4. The speed of sound c_{SAW} for each peak corresponding to the wavenumber is also shown above the respective peak.

References

[1] H.J. Qiu, X. Li, H.T. Xu, H.J. Zhang, Y. Wang, Nanoporous metal as a platform for electrochemical and optical sensing, Journal of Materials Chemistry C. 2 (2014) 9788-9799.https://doi.org/10.1039/c4tc01913j

[2] J. van der Zalm, S. Chen, W. Huang, A. Chen, recent advances in the development of nanoporous Au for sensing applications, Journal of The Electrochemical Society. 167 (2020) 037532

[3] V. Zielasek, B. Jurgens, C. Schulz, J. Biener, M.M. Biener, A.V. Hamza, M. Baumer, Gold catalysts: Nanoporous gold foams, Angewandte Chemie-International Edition. 45 (2006) 8241-8244.https://doi.org/10.1002/anie.200602484

[4] M.L. Sun, K. Han, R. Hu, D. Liu, W.Z. Fu, W.M. Liu, Advances in Micro/Nanoporous Membranes for Biomedical Engineering, Advanced Healthcare Materials. 10 (2021).https://doi.org/10.1002/adhm.202001545

[5] Y. Ding, Z. Zhang, Nanoporous metals for advanced energy technologies, Springer, 2016.

[6] H. Shao, Y.C. Wu, Z.F. Lin, P.L. Taberna, P. Simon, Nanoporous carbon for electrochemical capacitive energy storage, Chemical Society Reviews. 49 (2020) 3005-3039.https://doi.org/10.1039/d0cs00059k

[7] A. Yadav, M. Muthukumar, M.S. Bobji, Tuning dendritic structure at nanoporous alumina/aluminium interface for uniform electrodeposition of metals for nanocomposite coatings, Surfaces and Interfaces. 24 (2021).https://doi.org/10.1016/j.surfin.2021.101115

[8] D. Petukhov, K. Napolskii, A. Eliseev, Permeability of anodic alumina membranes with branched channels, Nanotechnology. 23 (2012) 335601

[9] M. Tian, S. Xu, J. Wang, N. Kumar, E. Wertz, Q. Li, P.M. Campbell, M.H. Chan, T.E. Mallouk, Penetrating the oxide barrier in situ and separating freestanding porous anodic alumina films in one step, Nano Letters. 5 (2005) 697-703

[10] O. Jessensky, F. Müller, U. Gösele, Self-organized formation of hexagonal pore arrays in anodic alumina, Applied physics letters. 72 (1998) 1173-1175

[11] J.T. Domagalski, E. Xifre-Perez, L.F. Marsal, Recent Advances in Nanoporous Anodic Alumina: Principles, Engineering, and Applications, Nanomaterials. 11 (2021).https://doi.org/10.3390/nano11020430

[12] N.M. Chelliah, A. Saxena, K. Sharma, H. Singh, M. Surappa, Surface characterization of nanoporous aluminium oxide films synthesized by single-step DC and AC anodization, Surfaces and Interfaces. 7 (2017) 139-145

[13] F. Keller, M. Hunter, D. Robinson, Structural features of oxide coatings on aluminum, Journal of the Electrochemical Society. 100 (1953) 411

[14] M. Kushwaha, A. Sil, S. Ray, Carbon nanotube/nanofiber embedded nanoporous anodized aluminium oxide surface and its tribological properties, Journal of Nanoscience and Nanotechnology. 8 (2008) 4152-4158

[15] F.A. Bruera, G.R. Kramer, M.L. Vera, A.E. Ares, Evaluation of the influence of synthesis conditions on the morphology of nanostructured anodic aluminum oxide coatings on Al 1050, Surfaces and Interfaces. 18 (2020).https://doi.org/10.1016/j.surfin.2020.100448

[16] M. Zhai, A. Locquet, M. Jung, D. Woo, D.S. Citrin, Characterization of nanoporous Al2O3 films at terahertz frequencies, Optics Letters. 45 (2020) 4092-4095.https://doi.org/10.1364/ol.390129

[17] M. Zhai, A. Locquet, M. Jung, D. Woo, D.S. Citrin, Nondestructive characterization of nanoporous alumina films using terahertz scattering imaging, Surface & Coatings Technology. 408 (2021).https://doi.org/10.1016/j.surfcoat.2020.126792

[18] B. Hosten, M. Deschamps, B.R. Tittmann, Inhomogeneous wave generation and propagation in lossy anisotropic solids - application to the characterization of viscoelastic composite-materials, Journal of the Acoustical Society of America. 82 (1987) 1763-1770.https://doi.org/10.1121/1.395170
[19] S.I. Rokhlin, W. Wang, Double through-transmission bulk wave method for ultrasonic phase-velocity measurement and determination of elastic-constants of composite-material, Journal of the Acoustical Society of America. 91 (1992) 3303-3312.https://doi.org/10.1121/1.402847
[20] D.A.P. Paterson, W. Ijomah, J.F.C. Windmill, Elastic constant determination of unidirectional composite via ultrasonic bulk wave through transmission measurements: A review, Progress in Materials Science. 97 (2018) 1-37.https://doi.org/10.1016/j.pmatsci.2018.04.001
[21] S.T. Rakotonarivo, C. Payan, J. Moysan, C. Hochard, Local damage evaluation of a laminate composite plate using ultrasonic birefringence of shear wave, Composites Part B-Engineering. 142 (2018) 287-292.https://doi.org/10.1016/j.compositesb.2018.01.006
[22] P. Zinin, O. Lefeuvre, G.A.D. Briggs, B.D. Zeller, P. Cawley, A. Kinloch, X.R. Zhou, G. Thompson, Determination of density and elastic constants of a thin phosphoric acid-anodized oxide film by acoustic microscopy, Journal of the Acoustical Society of America. 106 (1999) 2560-2567.https://doi.org/10.1121/1.428087
[23] J. Chen, X.L. Bai, K.J. Yang, B.F. Ju, Simultaneously measuring thickness, density, velocity and attenuation of thin layers using V(z, t) data from time-resolved acoustic microscopy, Ultrasonics. 56 (2015) 505-511.https://doi.org/10.1016/j.ultras.2014.09.019
[24] S.I. Rokhlin, W. Wang, Measurements of elastic-constants of very thin anisotropic plates, Journal of the Acoustical Society of America. 94 (1993) 2721-2730.https://doi.org/10.1121/1.407355
[25] B.W. Maxfield, An acoustic microscope for surface coating characterization, IEEE Transactions on Sonics and Ultrasonics. 29 (1982) 178-179
[26] Y. Tsukahara, Y.S. Liu, C. Neron, C.K. Jen, J. Kushibiki, Longitudinal critical angle singularities and their effect on v(z) of the line-focus-beam acoustic microscope, IEEE Transactions on Ultrasonics Ferroelectrics and Frequency Control. 41 (1994) 458-466.https://doi.org/10.1109/58.294105
[27] M.G. Somekh, H.L. Bertoni, G.A.D. Briggs, N.J. Burton, A two-dimensional imaging theory of surface discontinuities with the scanning acoustic microscope, Proceedings of the Royal Society of London Series a-Mathematical Physical and Engineering Sciences. 401 (1985) 29-51.https://doi.org/10.1098/rspa.1985.0086
[28] I. Ishikawa, H. Kanda, K. Katakura, T. Semba, Measurement of a damaged layer thickness with reflection acoustic microscope, IEEE Transactions on Ultrasonics Ferroelectrics and Frequency Control. 36 (1989) 587-592.https://doi.org/10.1109/58.39108
[29] R.A. Al-Juboori, V. Aravinthan, T. Yusaf, Impact of pulsed ultrasound on bacteria reduction of natural waters, Ultrason Sonochem. 27 (2015) 137-147.https://doi.org/10.1016/j.ultsonch.2015.05.007
[30] J.-I. Kushibiki, N. Chubachi, Material characterization by line-focus-beam acoustic microscope, IEEE transactions on sonics and ultrasonics. 32 (1985) 189-212
[31] R. Weglein, A model for predicting acoustic material signatures, Applied Physics Letters. 34 (1979) 179-181
[32] A. Atalar, A physical model for acoustic signatures, Journal of Applied Physics. 50 (1979) 8237-8239
[33] O. Marangos, A. Misra, Modeling micromechanical measurements of depth-varying properties with scanning acoustic microscopy, Continuum Mechanics and Thermodynamics. 30 (2018) 953-

976.https://doi.org/10.1007/s00161-018-0625-y
[34] W. Lee, The Anodization of Aluminum for Nanotechnology Applications, Jom. 62 (2010) 57-63.https://doi.org/10.1007/s11837-010-0088-5
[35] M.S. Ilango, A. Mutalikdesai, S.K. Ramasesha, Anodization of Aluminium using a fast two-step process, Journal of Chemical Sciences. 128 (2016) 153-158.https://doi.org/10.1007/s12039-015-1006-8
[36] R.G. Maev, Advances in acoustic microscopy and high resolution imaging: from principles to applications, John Wiley & Sons, 2013.
[37] E.T.A. Mohamed, J.-M. Perone, S. Brand, M. Koegel, N.F. Declercq, Scanning Acoustic Microscopy Comparison of Descemet's Membrane Normal Tissue and Tissue With Fuchs' Endothelial Dystrophy, Investigative Ophthalmology & Visual Science. 59 (2018) 5627-5632
[38] W. Li, J.D. Achenbach, V(z) measurement of multiple leaky wave velocities for elastic constant determination, Journal of the Acoustical Society of America. 100 (1996) 1529-1537.https://doi.org/10.1121/1.416033
[39] A. Briggs, Advances in acoustic microscopy, Springer Science & Business Media, 2013.
[40] S.Z. Zhang, X.B. Li, H. Jeong, Measurement of Rayleigh Wave Beams Using Angle Beam Wedge Transducers as the Transmitter and Receiver with Consideration of Beam Spreading, Sensors. 17 (2017).https://doi.org/10.3390/s17061449
[41] B. Zeller, A. Kinloch, P. Cawley, P. Zinin, G. Briggs, G. Thompson, X. Zhou, Adhesive/adherend interlayer property measurement by acoustic microscopy, in: Review of Progress in Quantitative Nondestructive Evaluation, Springer, 1997, pp. 1237-1244.
[42] M. Breazeale, L. Adler, G.W. Scott, Interaction of ultrasonic waves incident at the Rayleigh angle onto a liquid-solid interface, Journal of Applied Physics. 48 (1977) 530-537
[43] W.G. Farnell, Types and properties of surface, Acoustic surface waves. (1978) 13-60
[44] B. Kovic, M. Lowe, DISPERSE user's manual version 2.0. 16B Imperial College, University of London, Non-Destructive Testing Laboratory. (2003)
[45] S.H. Gong, A. Stolz, G.H. Myeong, E. Dogheche, A. Gokarna, S.W. Ryu, D. Decoster, Y.H. Cho, Effect of varying pore size of AAO films on refractive index and birefringence measured by prism coupling technique, Optics Letters. 36 (2011) 4272-4274.https://doi.org/10.1364/ol.36.004272
[46] G.A.D. Briggs, O.V. Kolosov, A. Briggs, O. Kolosov, Experimental elastic microanalysis, in: Acoustic Microscopy, Oxford University Press, 2009, pp. 0.